PHYSICAL REVIEW B **79**, 155420 (2009)

Nonlinear Mie theory for second-harmonic and sum-frequency scattering

Alex G. F. de Beer* and Sylvie Roke†
Max Planck Institute for Metals Research, Heisenbergstrasse 3, D70569 Stuttgart, Germany

(Received 17 November 2008; revised manuscript received 6 February 2009; published 14 April 2009)

We present a theory for second-order nonlinear light scattering from spherical particles using source waves of arbitrary frequency and direction based on a combination of linear Mie scattering and reciprocity theory. The theory presented in this work extends existing theory applied to second-harmonic scattering by allowing noncollinear excitation waves of unequal frequency. The absence of an intrinsic symmetry axis was overcome by using a nonstandard expansion for the linear interaction. Numerical results obtained for water droplets in air show an increase in the number of observed maxima in the sum-frequency scattering pattern compared to index-matched theories, as well as a strong backscatter peak, which eventually dominates the scattering pattern. Our method opens up possibilities for studying increasingly complex colloidal systems with nonlinear light scattering spectroscopy.

DOI: 10.1103/PhysRevB.79.155420 PACS number(s): 78.68.+m, 42.65.−k, 82.70.Dd

I. INTRODUCTION

Nonlinear light scattering (NLS) is a combination of light scattering and nonlinear optics. In the case of second-order techniques NLS allows for the *in situ* study of nonplanar surfaces, such as micro- and nanoscopic particles in a suspension. Electronically enhanced surface resonances were measured with second harmonic generation (SHG) scattering to probe the adsorption behavior of (dye) molecules on particle surfaces in (soft) condensed media.[1–10] In these studies colloidal dispersions were illuminated by a single pulsed laser beam, and the generated second-harmonic (SH) light was detected in a wide angle in the direction of the laser beam. Also, it was recognized that the angular dependence of the scattered light holds information on the physical origin of the scattering process and the size and shape of the particles.[2] To model the scattered light several approximations can be used, such as the Rayleigh-Gans-Debye (RGD) approximation,[2,11–20] the small particle (electrostatic) limit[16,21–32] and the small index contrast [Wentzel-Kramers-Brillouin (WKB)] limit.[16,19] An exact theory, nonlinear Mie theory, has also been proposed.[33] Although exact, this treatment relies on the existence of a cylindrical symmetry axis, which is only the case in a collinear experimental setup.

Vibrational resonances of surfaces of dispersed particles can be measured with vibrational sum-frequency generation (SFG). This allows us to extract information from the vibrational surface spectrum, which can be recorded at each scattering angle. The resulting data then contain information about the chemical structure, orientation, and order of molecules on the particle surface.[15,20,34,35] An exact theoretical description for this type of scattering does not exist. Although analogous to that of SHG scattering, this description is complicated by the fact that the employed laser beams are typically different in frequency, propagation direction, and propagation velocity. The absence of double degeneracy interferes with the requirement for cylindrical symmetry for the SHG scattering theory. Thus, a revision of the theoretical treatment is required.

An exact treatment would be extremely valuable because it allows for a description of any linear light-matter interaction with *any* type of surface second-order nonlinear light scattering process as long as the particle is spherical so that a diverse range of NLS processes can be described. This would be of use for the study of complex colloidal systems such as metallic, semiconductor, and biological particles embedded in condensed media.

Here, we present an approach that allows us to calculate nonlinear Mie scattering for noncollinear NLS, with incoming beams that have a difference in frequency (i.e., complete absence of degeneracy). The absence of cylindrical symmetry in the propagation direction requires an alternative expansion of the local electric fields. This expansion is accomplished by choosing spherical coordinates with respect to the axis perpendicular to all propagation directions. Knowing the fields at the surface, we proceed to calculate the exact scattered far field by applying the reciprocity theorem. We end by comparing our model to several known approximations and calculate NLS patterns from water droplets in air.

II. THEORY

Nonlinear optical effects are usually described in terms of a multipolar expansion of the nonlinear polarization, which is generated by the interaction of the incoming electromagnetic fields with a material. The leading order of this expansion, the electric dipole contribution, is nonvanishing at interfaces or in a noncentrosymmetric bulk. The magnitude of this second-order polarization $\mathbf{P}^{(2)}$ is determined by the nonlinear susceptibility following the relation $P_i^{(2)}=\chi_{ijk}^{(2)}E_{1,j}E_{2,k}$. The numerical subscripts (0,1,2) denote the participating fields by order of decreasing wavelength so that the sum-frequency field is denoted by the index 0.

The nonlinear polarization depends on the local field strengths of the incoming waves. For collinear SHG, a single electromagnetic field is taken as the source, but for SFG two waves with a different frequency are combined, which are generally noncollinear and possess different propagation speeds inside the particle. We describe the incoming fields as plane waves of the type $\mathbf{E}=E\mathbf{u}e^{i(\mathbf{k}\cdot\mathbf{r}-\omega t)}$, where E is the field amplitude, $\mathbf{u}$ is the unit polarization vector, $\mathbf{k}$ is the wave vector, and ω is the angular frequency of the field. At the surface of the particle, these fields are modified due to linear optical interactions, which depend on the different frequencies of the fields. It is these distorted fields that contribute to the nonlinear polarization.

Once the local fields and the nonlinear polarization are known, it is possible to calculate the scattering pattern in the far field. This can be done by solving the nonlinear boundary conditions at the particle surface and subsequently calculating the signal in the far field as has been done in the case of SHG Mie scattering.[33] Some controversy remains, however, as to the correct form of these boundary conditions[27,36]

Alternatively, the scattering pattern can be calculated by applying the reciprocity theorem[16,37] which circumvents the need to consider nonlinear near field interactions. In short, the reciprocity theorem is based on the principle of time reversal of electromagnetic waves: the light emitted from a polarization distribution $\mathbf{P}$ will, at a point of detection $\mathbf{r}_0$ in the far field, resemble a spherical wave. Time reversal suggests that this is equivalent to a spherical wave returning from the direction of $\mathbf{r}_0$, which induces a (linear) polarization itself. The integrated inner product of this returning electromagnetic wave $\mathbf{E}'$ with the original polarization can therefore be interpreted as the extent to which a polarization $\mathbf{P}$ contributes to a far-field signal in the direction of $\mathbf{r}_0$. In the case of a scattering particle, the reciprocity relation is formally given by[16]

$$\mathbf{E}(r_0)\cdot\mathbf{u} = e^{ik_0r_0}\frac{k_0^2}{r_0}\int i\omega\mathbf{P}\cdot\boldsymbol{E}'d^3\mathbf{r}', \qquad (1)$$

where $\mathbf{E}$ is the (real) electromagnetic wave arriving in the far field, k_0 is its wave number, and $\mathbf{E}'$ is the theoretical returning spherical wave from the direction of $\mathbf{r}_0$, which is subject to regular linear interactions. The integration is taken over the volume of the particle ($d^3\mathbf{r}'$).

For the purpose of a nonlinear light scattering experiment, $\mathbf{P}$ takes the form of the nonlinear polarization $\mathbf{P}^{(2)}$ that is the result of the interactions of the two incoming source fields with the surface region (given by $P_i^{(2)}=\chi_{ijk}^{(2)}E_{1,j}E_{2,k}$). $\mathbf{E}(r_0)$ is the sum-frequency field arriving at the detector, and $\mathbf{E}'$ is the time-reversed counterpart of $\mathbf{E}$ (i.e., a spherical wave coming in from the position of the detector with wave number k_0). The reciprocity relation then results in an almost symmetrical interaction between three linear electromagnetic near fields as follows:

$$\mathbf{E}_0(r_0)\cdot\mathbf{u} = i\omega_0 e^{ik_0r_0}\frac{k_0^2}{r_0}\int\sum_{j,k,l}E'_{0,j}(\mathbf{r}')\chi_{jkl}^{(2)}(\mathbf{r}')$$
$$\times E_{1,k}(\mathbf{r}')E_{2,l}(\mathbf{r}')d^3\mathbf{r}', \qquad (2)$$

where it should be noted that $\mathbf{E}_0'$ is a unity amplitude field.

The emitted electric field can therefore be obtained by considering the linear interactions of three incoming waves—two for the source wave and one for the returning wave at the nonlinear frequency—and combining the results using the nonlinear susceptibility tensor. The reciprocity treatment circumvents nonlinear boundary conditions and shows the symmetric relation between source and nonlinear electromagnetic fields. To obtain the nonlinear scattering pattern, the first step is to obtain expressions for each of the individual electromagnetic near fields separately.

A. Local fields

An exact solution for the electric field at the surface of a dielectric particle is given by linear Mie theory.[38] Many different but equivalent treatments of the theory exist in literature,[38–44] which vary slightly but are all based on the same concept: an expansion of the electric field into vector spherical harmonics (VSH) is used for the incoming field, which is then coupled to an internal and a scattered field using boundary conditions that follow from the Maxwell equations.

We use an orthogonal expansion in spherical coordinates in terms of the spherical harmonics Y_{lm}. The local electromagnetic field can be represented as

$$\mathbf{E} = \sum_{lm}A_{lm}\mathbf{M}_{lm} + B_{lm}\mathbf{N}_{lm}, \qquad (3)$$

$$\mathbf{M}_{lm} = j_l(nkr')\frac{1}{\sin\,\theta'}\frac{dY_{lm}(\theta',\phi')}{d\phi'}\mathbf{e}_{\theta'}$$
$$- j_l(nkr')\frac{dY_{lm}(\theta',\phi')}{d\theta'}\mathbf{e}_{\phi'}, \qquad (4)$$

$$\mathbf{N}_{lm} = l(l+1)\frac{j_l(nkr')Y_{lm}(\theta',\phi')}{nkr'}\mathbf{e}_{r'}$$
$$+\frac{d[r'j_l(nkr')]}{nkr'dr'}\frac{dY_{lm}(\theta',\phi')}{d\theta'}\mathbf{e}_{\theta'}$$
$$+\frac{d[r'j_l(nkr')]}{nkr'dr'}\frac{1}{\sin\,\theta'}\frac{dY_{lm}(\theta',\phi')}{d\phi'}\mathbf{e}_{\phi'}, \qquad (5)$$

where we have temporarily dropped the subscripts (0,1,2) for convenience. Here, j_l is a spherical Bessel function of the first kind and should be replaced by a spherical Hankel function of the first kind (h_l) for the scattered field, k is the wave number, and n is the index of refraction of the particle divided by that of the medium. Y_{lm} is the spherical harmonic function. The coordinates r', θ', and ϕ' are spherical coordinates with respect to the particle center and a symmetry axis. Usually this axis is chosen to be lined up with the incoming field (the z axis), reducing the expansion coefficients A_{lm} and B_{lm} to simple expressions that are both nonzero only[42] for $m=\pm 1$.

Here, however, our aim is to describe scattering from a set of noncollinear waves, and we have to use a less common orientation, perpendicular to the direction of incidence: we take the y axis as polar axis (see Fig. 1). This results in a more complicated expansion of coefficients A_{lm} and B_{lm} but this is traded off by a more convenient expression for rotation around the y axis, which for this expansion can be conveniently obtained for an arbitrary angle ζ by multiplying each coefficient with a factor $e^{im\zeta}$. The expansion terms for a plane wave traveling along the positive z axis are[45]

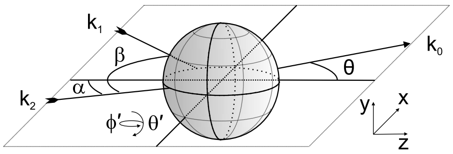

FIG. 1. Overview of the relevant parameters in the model: the sum frequency and source waves have k vectors $\mathbf{k}_0$, $\mathbf{k}_1$, and $\mathbf{k}_2$ in order of decreasing frequency. The angle between the propagation direction of the lowest frequency wave and the positive z axis is α, the opening angle between source waves β. Local fields are expressed in spherical coordinates (r',θ',ϕ'), which are defined with respect to the y axis. The sum-frequency scattering pattern is parametrized using the scattering angle θ.

$$A_{lm}^{\mathrm{inc}} = \frac{2\pi i^{l+1}}{l(l+1)}\Big[\sqrt{(l+m+1)(l-m)}\,Y_{lm+1}^{*}(\pi/2,\pi/2) + \sqrt{(l-m+1)(l+m)}\,Y_{lm-1}^{*}(\pi/2,\pi/2)\Big], \tag{6}$$

$$B_{lm}^{\mathrm{inc}} = \frac{4\pi i^{l}}{l(l+1)} m Y_{lm}^{*}(\pi/2,\pi/2), \tag{7}$$

for a polarization along the x axis (p polarization). For polarization along the y axis (s polarization), the expansion coefficients have to be interchanged and multiplied by an additional complex phase factor i.

Unchanged from original Mie theory, the incoming electromagnetic field ($\mathbf{E}^{\mathrm{inc}}$) can now be coupled to the field inside the particle ($\mathbf{E}^{\mathrm{part}}$) and the scattered field ($\mathbf{E}^{\mathrm{scat}}$) by using the boundary conditions for the case of linear light-matter interaction,[40]

$$\mathbf{r}' \times (\mathbf{E}^{\mathrm{inc}} + \mathbf{E}^{\mathrm{scat}}) = \mathbf{r}' \times \mathbf{E}^{\mathrm{part}}, \tag{8}$$

$$\mathbf{r}' \times (\mathbf{H}^{\mathrm{inc}} + \mathbf{H}^{\mathrm{scat}}) = \mathbf{r}' \times \mathbf{H}^{\mathrm{part}}, \tag{9}$$

which for the internal field gives expansion coefficients

$$A_{lm}^{\mathrm{part}} = A_{lm}^{\mathrm{inc}} \left. \frac{j_l(kr')\dfrac{\partial r' h_l(kr')}{\partial r'} - h_l(kr')\dfrac{\partial r' j_l(kr')}{\partial r'}}{j_l(nkr')\dfrac{\partial r' h_l(kr')}{\partial r'} - h_l(kr')\dfrac{\partial r' j_l(nkr')}{\partial r'}} \right|_{(r'=R)}, \tag{10}$$

$$B_{lm}^{\mathrm{part}} = B_{lm}^{\mathrm{inc}} \left. \frac{n j_l(kr')\dfrac{\partial r' h_l(kr')}{\partial r'} - n h_l(kr')\dfrac{\partial r' j_l(kr')}{\partial r'}}{n^2 j_l(nkr')\dfrac{\partial r' h_l(kr')}{\partial r'} - h_l(kr')\dfrac{\partial r' j_l(nkr')}{\partial r'}} \right|_{(r'=R)}, \tag{11}$$

where R is the radius of the spherical particle.

The nonlinear surface process takes place on a thin film on the outside of the particle surface. The local electric field on the outside surface is equal to the internal field $\mathbf{E}^{\mathrm{part}}$ in the direction of θ' and ϕ'. The radial part needs to be adjusted for the jump of the electric field across the interface by a factor of the dielectric constant $\epsilon = n^2$. This expansion has to be obtained for each of the incoming fields at the three frequencies involved.

B. Nonlinear polarization

The next step in obtaining an expression for nonlinear scattering pattern is combining the three near fields with the nonlinear susceptibility tensor $\boldsymbol{\chi}^{(2)}$. For an electric dipole contribution, the scattering amplitude is given by

$$\mathbf{E}_0(r_0)\cdot\mathbf{u} = i\omega_0 e^{ik_0 r_0}\frac{k_0^2}{r_0}\int \sum_{j,k,l} E'_{0,j}(\mathbf{r}')\chi_{jkl}^{(2)}(\mathbf{r}') \times E_{1,k}(\mathbf{r}')E_{2,l}(\mathbf{r}')d^3\mathbf{r}', \tag{12}$$

where each of the electric near fields is represented by an expansion in VSHs. In a centrosymmetric medium $\boldsymbol{\chi}^{(2)}$ vanishes in the bulk. The nonlinear susceptibility will therefore be of the form $\boldsymbol{\chi}^{(2)} = \boldsymbol{\chi}_{\mathrm{surf}}^{(2)}\delta(r'-R)$, which reduces the above expression to a surface integral.

The nonlinear susceptibility tensor of a surface follows the local curvature of the surface. For a spherical particle with an isotropic surface and with a curvature that is large compared to the atomic scale, this surface has a local C_∞ symmetry. In this case, the nonvanishing $\boldsymbol{\chi}^{(2)}$ elements are $\chi_{\perp\perp\perp}^{(2)}$, $\chi_{\perp\|\|}^{(2)}$, $\chi_{\|\perp\|}^{(2)}$, $\chi_{\|\|\perp}^{(2)}$, $\chi_{\perp\|\|'}^{(2)} = -\chi_{\perp\|'\|}^{(2)}$, $\chi_{\|\|'\perp}^{(2)} = -\chi_{\|'\|\perp}^{(2)}$, and $\chi_{\|'\perp\|}^{(2)} = -\chi_{\|\perp\|'}^{(2)}$,[46] where $\perp$, $\|$, and $\|'$ denote the perpendicular and two mutually orthogonal parallel directions with respect to the local surface so that $(\perp,\|,\|')$ forms a right-handed coordinate system. For such a surface, the number of independent nonvanishing tensor components is seven. In the presence of a plane of mirror symmetry, the number of independent components is reduced to four. Since $\boldsymbol{\chi}^{(2)}$ can be related to the molecular hyperpolarizability $\boldsymbol{\beta}^{(2)}$, the relative magnitudes of the susceptibility tensor elements contain information on molecular orientation.[47]

The first nonvanishing terms in a centrosymmetric bulk material are the electric quadrupole and magnetic dipole contributions. Distinguishing the higher-order bulk contributions from those of the surface dipole remains a challenge due to the nonuniqueness in separation between the two.[48,49] The pure surface contribution can only be isolated when higher-order contributions are negligible compared to those of the surface dipole. An analysis by Held *et al.*[50] showed separation is possible when either thickness of the molecular surface layer is large compared to the size of an electronic wave function or vibrational amplitude or in cases where there is a distinct difference in directionality between the molecules at the surface and in the bulk. Also, when spectroscopic differences exist between bulk and surface, the different contributions can be separated. Additionally, in a dispersion the ratio of surface molecules to bulk molecules is increased compared to a planar interface. A possible contribution from a quadrupole term will therefore be much smaller in a scattering experiment compared to an experiment conducted on a planar interface. Though a treatment of the bulk quadrupole contribution to the nonlinear scattering signal is of interest, a full analysis is beyond the scope of this paper. We will, for the remainder of this paper, assume that the higher-order bulk contributions are negligible compared to the electric dipole surface contribution. A short treatment of the formalism for quadrupole scattering is given in the Appendix.

For a spherical particle, an isotropic surface locally has a C_∞ symmetry so that only the components $\chi^{(2)}_{\perp\perp\perp}$, $\chi^{(2)}_{\perp\parallel\parallel}$, and $\chi^{(2)}_{\perp\parallel\parallel'}$ and their index permutations can have nonvanishing contributions. When these terms are combined, only three different types of integral arise from the combinations of **M** and **N**,

$$U^{ll'l''}_{mm'm''} = \int_0^{2\pi}\int_0^{\pi} Y_{lm}Y_{l'm'}Y_{l''m''}\sin\theta' d\theta' d\phi', \tag{13}$$

$$V^{ll'l''}_{mm'm''} = \int_0^{2\pi}\int_0^{\pi} Y_{lm}\left(\frac{dY_{l'm'}}{d\theta'}\frac{dY_{l''m''}}{d\phi'} - \frac{dY_{l'm'}}{d\phi'}\frac{dY_{l''m''}}{d\theta'}\right)d\theta' d\phi', \tag{14}$$

$$W^{ll'l''}_{mm'm''} = \int_0^{2\pi}\int_0^{\pi} Y_{lm}\left(\frac{dY_{l'm'}}{d\theta'}\frac{dY_{l''m''}}{d\theta'} + \csc^2\theta' \frac{dY_{l'm'}}{d\phi'}\frac{dY_{l''m''}}{d\phi'}\right) \times\sin\theta' d\theta' d\phi'. \tag{15}$$

As an example, for polarization combination *ppp* (all polarizations parallel to the plane of scattering) the part involving $\chi^{(2)}_{\perp\parallel\parallel}$ generates the following expression:

$$\begin{aligned} E_{0,ppp} = \chi^{(2)}_{\perp\parallel\parallel} \sum_{ll'l''mm'm''} n_0 \frac{l(l+1)B^{\text{part}}_{0,lm}j_{0,l}}{k_0R} e^{i[m\theta+m'(\alpha-\beta)+m''\alpha]} \\ \times[(B^{\text{part}}_{1,l'm'}A^{\text{part}}_{2,l''m''}j'_{1,l'}j_{2,l''} \\ - A^{\text{part}}_{1,l'm'}B^{\text{part}}_{2,l''m''}j_{1,l'}j'_{2,l''})V^{ll'l''}_{mm'm''} \\ + (A^{\text{part}}_{1,l'm'}A^{\text{part}}_{2,l''m''}j_{1,l'}j_{2,l''} \\ + B^{\text{part}}_{1,l'm'}B^{\text{part}}_{2,l''m''}j'_{1,l'}j'_{2,l''})W^{ll'l''}_{mm'm''}]. \end{aligned} \tag{16}$$

Here, j'_l is short for $\frac{d[r'z_l(nkr')]}{nkr'dr'}$ and the subscripts (0,1,2) again denote the waves with different frequency. The angles α and β determine the scattering geometry: α is the angle of the lowest frequency wave with the forward-scattering direction, and β is the opening angle between the source waves. Finally, θ is the scattering angle (see Fig. 1). The term $\exp\{i[m\theta+m'(\alpha-\beta)+m''\alpha]\}$ is a basic property of scattering: we can interpret the angular dependence of Eq. (16) as a Fourier series of the type $\Sigma C_m e^{im\theta}$, which means that for higher expansion numbers l (which restrict the maximum value of m), sharper features may appear in the scattering pattern.

The integrals U, V, and W have been evaluated in studies relating to geomagnetism and meteorology and can be described as products of Wigner $3j$ and $6j$ symbols,[51–53]

$$U^{ll'l''}_{mm'm''} = \sqrt{\frac{(2l+1)(2l'+1)(2l''+1)}{4\pi}}\begin{pmatrix} l & l' & l'' \\ m & m' & m'' \end{pmatrix} \times\begin{pmatrix} l & l' & l'' \\ 0 & 0 & 0 \end{pmatrix}, \tag{17}$$

$$\begin{aligned} V^{ll'l''}_{mm'm''} = -i\sqrt{\frac{(2l+1)(2l'+1)(2l''+1)}{4\pi}} \\ \times\sqrt{\frac{(l+l'+l''+2)(l+l'+l''+4)}{4(l+l'+l''+3)}} \\ \times\sqrt{(l+l'-l''+1)(l-l'+l''+1)}\sqrt{(-l+l'+l''+1)} \\ \times\begin{pmatrix} l & l' & l'' \\ m & m' & m'' \end{pmatrix}\begin{pmatrix} l+1 & l'+1 & l''+1 \\ 0 & 0 & 0 \end{pmatrix}, \end{aligned} \tag{18}$$

$$\begin{aligned} W^{ll'l''}_{mm'm''} = -\sqrt{\frac{(2l+1)(2l'+1)(2l''+1)}{4\pi}} \\ \times\sqrt{l'(l'+1)l''(l''+1)(2l'+1)(2l''+1)}\begin{Bmatrix} l' & l' & 1 \\ l'' & l'' & l \end{Bmatrix} \\ \times\begin{pmatrix} l & l' & l'' \\ m & m' & m'' \end{pmatrix}\begin{pmatrix} l & l' & l'' \\ 0 & 0 & 0 \end{pmatrix}. \end{aligned} \tag{19}$$

A converging solution requires summation over all possible combinations of l, l', l'', m, m' and m'' up to a maximum value $l = l_{\max}$. The total number of summation terms that is required therefore grows with $l_{\max}$ as $l^6_{\max}$. The cutoff value increases linearly with particle size so that for large particles computation times become extremely large. In practice, for particles larger than $k_0R=5$ it is much faster to calculate the linear electromagnetic fields for a large set of points at the particle surface and numerically integrate them for the correct scattering amplitude rather than relying on the analytical expression.

III. NUMERICAL RESULTS

We used custom written Matlab routines to generate the required Legendre polynomials and Bessel coefficients. Using these coefficients, a program was written in C#, a programming language similar to C++ and JAVA. This program calculates radial and tangential components of the linear surface electric fields for a set of points on the particle surface. The source fields were then combined into a nonlinear surface polarization, which in turn was combined with the sum-frequency field. Rotations were achieved by shifting the surface points to eliminate the need for calculating a new field for every angle. Figure 2 shows the resultant field for a single calculation: here, the radial interactions (via $\chi^{(2)}_{\perp\perp\perp}$) of a low frequency wave (left picture) and higher frequency wave (middle picture) were combined to generate a nonlinear polarization (right picture). The calculations were accelerated by offloading all image calculations to the graphics processor. In this way, a full set of high-resolution scattering patterns (in all possible polarization combinations) could be generated within a few minutes on a regular desktop computer.

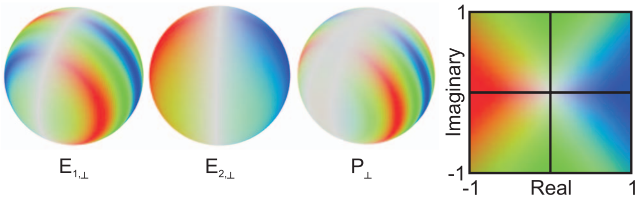

FIG. 2. (Color) Illustration of the nonlinear polarization built up by combining source waves of $\lambda_1=800$ nm and $\lambda_2=3447$ nm. The radial components of the local electric fields $\mathbf{E}_1$ and $\mathbf{E}_2$, represented by the left and middle spheres, couple according to the relation $P_\perp=\chi^{(2)}_{\perp\perp\perp}E_{1,\perp}E_{2,\perp}$, represented in the right sphere. The electric fields, as well as the polarization vary in phase (represented by color) and amplitude (represented by the saturation of the color). The inner product of the polarization with the sum-frequency wave yields the sum-frequency amplitude. For both source waves, a unity index of refraction was taken, though the procedure also applies for nonunity values. The rightmost image shows a legend for the colors used: blue and red correspond to positive and negative real components, while green corresponds to the amplitude of imaginary components.

A lower limit on the number of data points required to correctly resolve the local electric fields depends on the number of expansion terms used: as this number increases, the corresponding spherical harmonics harbor an increasing amount of oscillations that need to be represented accordingly. The number of expansion terms needed can be estimated by considering the value of $k_{0,1,2}R$: the expansion coefficients for the linear fields vary only minimally for $l < k_{0,1,2}R$ and drop off rapidly for $l > k_{0,1,2}R$, which provides a good estimate for an appropriate cutoff value $l_{\max}$. A discrete representation of the local electric field must be able to capture all oscillations contained in a expansion up to $l_{\max}$. In the ϕ' direction, for instance, this is determined by the spherical harmonic $Y_{lm}(\theta',\phi')$, which contains a factor $e^{im\phi'}$. In this direction, the maximum number of attainable oscillations is $m=l_{\max}$. According to the Nyquist criterion,[54] we therefore need at least $2l_{\max}$ data points to describe this oscillation.

The number of data points needed to describe the angular scattering intensity is also subject to a lower limit: the term $e^{i(m\theta+m'(\alpha-\beta)+m''\alpha)}$ in Eq. (16) oscillates with a frequency determined by m, the value of which is limited by $l_{\max}$. The number of angular samples to correctly represent a scattering pattern is therefore also determined by the Nyquist criterion: a sampling of at least $2l_{\max}$ scattering angles is required to correctly represent the pattern. For the largest radius ($R=1600$ nm) used in this article, a cutoff of $l_{\max}=30$ was used. The Nyquist criterion therefore requires a resolution of at least 60 pixels in the ϕ' direction to describe the electric field, as well as at least 60 angular samples of the scattering pattern. The resolution we used (512 pixels for both the electric field representation as well as the angular sampling of the scattering pattern) was well above these values.

A. Verification of the algorithm

Although no treatments exist for generalized nonlinear scattering from noncollinear sources of different frequency, a number of limiting cases exist for which exact, analytical solutions are available. These limiting cases allow us to verify the correctness of our algorithm. Exact treatments exist for negligible index of refraction differences ($\Delta n_{0,1,2} \approx 0$), where the RGD regime applies[16,18] as well as in the limit of small particles ($k_0R \ll 1$).[16,27] Moreover, using a collinear set of source waves of equal frequency should yield results that are in correspondence with earlier work on SHG scattering theory.

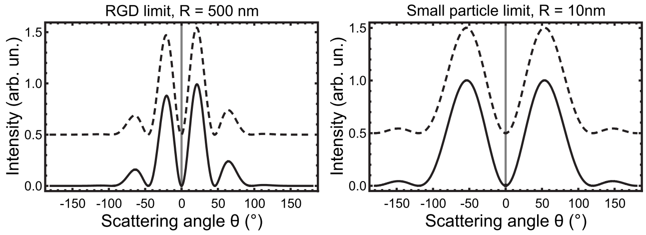

FIG. 3. Comparison of results obtained with numerical Mie simulation to previous analytical expressions: (a) Scattering pattern of sum-frequency generation by source beams at an opening angle β of 15° for which $\lambda_1=800$ nm and $\lambda_2=3447$ nm at the surface of a particle of radius $R=500$ nm, for which $\chi^{(2)}_{\perp\perp\perp}=1$. Numerical results (solid curve) correspond exactly to analytical results (dashed curve; offset for clarity). (b) Scattering pattern corresponding to the small particle limit ($R=10$ nm). A second-harmonic scattering pattern was simulated using a source wavelength of 800 nm and $\chi^{(2)}_{\perp\perp\perp}=1$ (solid curve), which corresponds exactly to analytical results in the small particle limit (dashed curve; offset for clarity). In both cases, the polarization combination was *ppp*.

In the first case, the RGD regime, interactions of the particle with the source fields are neglected and the surface field is taken as a plane wave. In the present theory, a negligible index of refraction causes the linear scattered wave to vanish. As a result, the electric field on the surface of the particle is equal to the incoming electric field. For vanishing index of refraction differences (for all three different wavelengths) the current theory is analytically identical to the RGD theory. In the RGD limit our Mie calculations should therefore correspond exactly to earlier RGD calculations.

Figure 3(a) shows a comparison to earlier presented scattering patterns.[18] Here, we simulated scattering for a sphere with radius $R=500$ nm, and a single $\boldsymbol{\chi}^{(2)}$ component $\chi^{(2)}_{\perp\perp\perp}=1$, using source waves of wavelength $\lambda_1=800$ nm and $\lambda_2=3447$ nm for the incoming waves, respectively, and polarization combination *ppp*. The opening angle β between the source waves was 15°; the index of refraction was set to unity for all wavelengths. Figure 3(a) shows the scattering pattern as calculated with RGD theory[18] and compares it to the pattern calculated by our nonlinear Mie algorithm. As can be seen both patterns are identical, which confirms the assumptions based on the analytical expressions. These results also provide a validation for our approach: the asymmetry in the scattering pattern caused by the noncollinear geometry can only be obtained if a nonzero angle between source beams is allowed. In collinear NLS, no such opening angle is present, and all scattering patterns are symmetric as a result of the symmetry of the geometry.

Analytical expressions for the small particle limit have been derived for SHG scattering,[25,27] as well as in more gen-

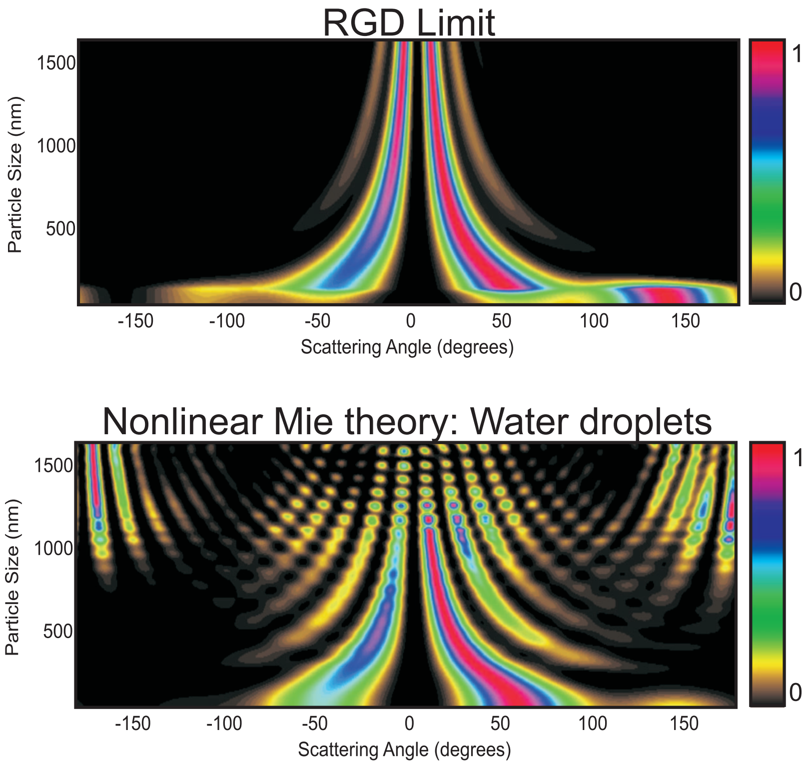

FIG. 4. (Color) Simulations of nonlinear scattering intensities for the *ppp* polarization as a function of scattering angle (horizontal axis) and particle size (vertical axis), using a noncollinear scattering setup consisting of source waves of wavelength $\lambda_1=800$ nm and $\lambda_2=2708$ nm under an angle at 15° with respect to each other. The topmost image shows scattering intensities in the case of a spherical particle of unity index of refraction $[(\Delta n_{0,1,2}\approx 0)]$, the bottom image those of spherical water droplets, with $n_0=1.33-1.3\cdot 10^{-8}i$, $n_1=1.33-1.25\cdot 10^{-7}i$, and $n_2=1.19-0.019i$. In both cases, the particle surfaces were chosen to be isotropic with $\boldsymbol{\chi}^{(2)}$ components taken from literature: $\chi^{(2)}_{\perp\perp\perp}=1$, $\chi^{(2)}_{\parallel\parallel\perp}=0.50+0.017i$, and $\chi^{(2)}_{\parallel\perp\parallel}=\chi^{(2)}_{\perp\parallel\parallel}=0.089-0.011i$. For clarity, each scattering pattern has been normalized to its peak intensity.

eral terms for other nonlinear processes.[16] Both treatments consider an expansion of the source fields into a leading-order term, a second-order term, and subsequent higher orders with respect to particle size. The leading-order term represents the electrostatic limit, whereas the second-order term represents the first correction to this limit. The scattering pattern is obtained by combining the expansions of source waves with the nonlinear wave. Combining the leading-order terms of the three expansions results in a vanishing contribution. The lowest nonvanishing terms are those that consist of a single second-order term (either from a source or a nonlinear wave) and two leading-order terms. For a collinear setup, this results in a scattering pattern consisting of a dipole term combined with a quadrupole term.[25,27] Our altered Mie expansion has no effect on the validity of this claim, and the results obtained in the small particle limit are identical. Figure 3(b) compares SHG scattering in the small particle limit to our Mie treatment, using $\chi^{(2)}_{\perp\perp\perp}=1$ and wavelengths of 800 and 400 nm for the source waves and sum-frequency wave, respectively. Here, as well as in the RGD limit, our Mie treatment corresponds exactly to analytical results.

B. Water droplets

In order to compare our model to earlier presented nonlinear Mie theories to describe SHG scattering, we have calculated SFG scattering patterns from water droplets in air.[33] SFG experiments on the planar water/air interface have shown that the vibrational SFG spectrum contains a single sharp peak at 3693 cm^{-1} and broader features at lower wave numbers.[55] The sharp peak at 3693 cm^{-1} is ascribed to a dangling OH-bond, a mode that can exist only at the interface. We have therefore simulated SFG scattering from spherical water droplets using wavelength $\lambda_1=800$ nm and $\lambda_2=2708$ nm ($\triangleq 3693$ cm^{-1}) and a resulting SFG wavelength of $\lambda_0=617$ nm. At these wavelengths, the bulk indices of refraction of water are[56] $n_0=1.33-1.3\cdot 10^{-8}i$ at the sum frequency, $n_1=1.33-1.25\cdot 10^{-7}i$ at the visible, and $n_2=1.19-0.019i$ at the infrared wavelength. The relative surface $\chi^{(2)}$ components were derived from experiments by Gan *et al.*[55] as $\chi^{(2)}_{\perp\perp\perp}=1$, $\chi^{(2)}_{\parallel\parallel\perp}=0.50+0.017i$, and $\chi^{(2)}_{\parallel\perp\parallel}=\chi^{(2)}_{\perp\parallel\parallel}=0.089-0.011i$.

Figure 4 shows scattering patterns as a function of particle size for two cases: the top image shows sum-frequency scattering in the RGD approximation, with indices of refraction set to unity for all wavelengths. The bottom image shows sum-frequency scattering from water droplets in air, using the wavelength-dependent indices of refraction of water.

The particle size increases from 10 (bottom of image) to 1600 nm (top of image). For clarity, every scattering pattern has been normalized to its respective peak value.

The number of expansion terms required for describing the electric field on a particle with nonunity index of refraction is determined by the value of $n_{0,1,2}k_{0,1,2}R$. An increased index of refraction therefore requires the inclusion of more expansion terms. This higher number of terms in turn causes a more sharply peaked scattering pattern compared to the RGD approximation. This effect can be clearly seen in Fig. 4: the first-order scattering peak, for instance, is much sharper and shifted further forward for water droplets than for the RGD approximation. Also, a larger fraction of the scattered energy is scattered to higher orders. In the RGD case, the amount of energy scattered in orders higher than the second is negligible, while water droplets cause the visibility of up to five distinct scattering orders.

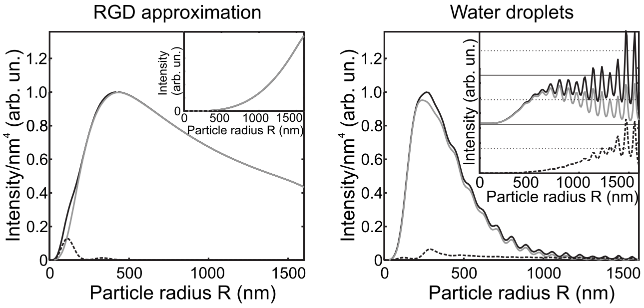

FIG. 5. Comparison of size-dependent integrated scattering intensities (solid black curves) as well intensities integrated over the forward (gray curves; −90 to 90°) and backward (dashed black curves; 90 to −90°) semicircle. The scattering geometry as well as the wavelength used were identical to those used in Fig. 4. All intensities have been divided by R^4 and normalized with respect to the resulting maximum value of the total scattered intensity. The insets show the same curves without dividing by R^4. In the case of water droplets, the curve has been offset for clarity. All graphs show values for the *ppp* polarization combination. The left graph represents the RGD limit. Here, the dominant backscattering contributions are due to initial appearance of first- and second-order scattering maxima, which appear at low radii and whose position shifts forward as the particle radius increases. At larger radii, the dominant scattering direction is forward. The graph on the right represents the intensities for water droplets. In the limit of small particles, the intensities follow a similar dependence on radius, though at larger radii a backscatter peak appears along with size-dependent oscillations in overall intensity due to shape resonances. At larger radii, the scattered energy is divided between forward and backward scatterings of which the backward contribution eventually dominates.

Another interesting aspect of these data is the presence of beats in the intensity. For scattering from larger droplets ($R = 1100-1600$ nm), the size can have a dramatic effect on the observed scattering pattern. These beats are most likely the result of shape resonance phenomena. Similar beats were also generated in the SH Mie calculations by Pavlyukh and Hübner.[33] The qualitative characteristics of our scattering patterns are in agreement with that work. We did, however, not attempt to recreate these values due to ongoing discussion on the correctness of the boundary conditions used in this paper.[27]

C. Total scattered intensity

Figure 5 shows the total intensity of in-plane scattered second-order light from a spherical particle (*ppp* polarization) in the case of the RGD approximation (left) and the exact, nonlinear Mie case for water droplets (right). In colloidal dispersions, the total scattered energy depends on the number of scattering centers, as well as the scattering cross section of a single particle. In the small particle limit ($k_0R < 1$), the surface polarization itself depends linearly on the radius[25] so that in this regime the scattering cross section follows a R^6 dependence. At larger sizes, we can expect that the nonlinear scattering cross section is proportional to the square of the surface area and therefore follows an R^4 dependence.

In Fig. 5 all intensity values have been divided by R^4 so that this power-law dependence can be quickly identified as being larger than (rising curve) or smaller than (falling curve) the R^4 dependency expected for a proportionality to surface area. Additionally, we have separated backscatter peaks from forward scattered peaks by plotting forward-scattering (gray curves; scattering angles between −90 and 90°) and backscattering (dashed curves; complementary angles) intensities. The insets show the same curves without the R^4 correction so that absolute scattered intensities can be compared.

In the RGD case (left), we can see that the three regimes lie in the ranges 0–250 nm for R^6 dependence and 250–500 nm for the R^4 dependence. At higher radii, the total intensity follows a power law of (slightly) less than 4. Light is scattered mainly in the forward direction. Even though two backscatter maxima can be observed for $R = 120$ nm and $R = 330$ nm, these are just the first-order scattering maximum and the second-order scattering maximum appearing at high angles and moving toward the forward direction (as can be seen in Fig. 4). In the Mie simulation for scattering from water droplets (Fig. 5, right), the total scattered intensity follows the same power law as the RGD case for small particle radii but rapidly drops below a R^4 dependence once particle size is larger than $R = 280$ nm. As size increases even further the total intensity shows large size-dependent oscillations, though the average value remains roughly constant.

The total backscattered intensity, though initially of smaller magnitude than the forward scattered intensity, remains closer to an R^4 dependence and eventually becomes larger than the forward scattering. As can be seen in Fig. 4 (bottom), the angular distribution of backscattered signal is concentrated in an angular range between 120 and −120° for radii above 1.4 μm and shows a trend toward even narrower distributions. At large particle sizes, for which resolving a scattering pattern experimentally may prove impractical, the integrated intensity in the backward angular range will still provide reliable size information.

IV. CONCLUSIONS

We have presented a method for calculating nonlinear light scattering using a Mie formalism for spherical particles in a general scattering setup consisting of noncollinear, nondegenerate source waves. The absence of appropriate symmetry conditions was compensated by expanding the electromagnetic source fields in a spherical coordinates system relative to an axis perpendicular to the propagations directions of both the source waves. The surface polarization could then be calculated from which the scattered electric field could be derived with reciprocity theory. Though in this work we limit this method to second-order processes, there is no limitation to the number of multiple-wave interactions to which it can be applied: as long as the nonlinear source term can be described by a surface polarization, the numerical algorithm can be applied directly by combining the larger number of interaction waves. Moreover, a bulk polarization can be treated in a similar way by an additional integration over the polarization in the radial direction. Furthermore, nonisotropic surfaces can be modeled by altering the components of $\boldsymbol{\chi}^{(2)}$ accordingly. Our simulations were verified in the limits for which previous results exist. We then compared scattering patterns of index-matched particles and water droplets as a function of particle size. In both cases, the scattering cross sections in the small particle limit were comparable, showing an R^6 dependence on particle radius. Clear differences in scattering patterns could be observed for larger particle radius ($k_0R > 5$): compared to the RGD limit, water droplets showed a sharper forward-peaked scattering pattern, a higher number of scattering side maxima, and a strong backscatter peak. In the case of water droplets, the scattering cross section follows a nontrivial oscillatory dependence on size, though the backscattered energy, which eventually dominates the cross section, shows an overall smoother dependence.

The noncollinear Mie theory presented in this work extends existing nonlinear Mie theory applied to second-harmonic scattering and allows for a theoretical description of two-beam SHG and SFG scattering experiments. As such, it opens up additional possibilities for the study of increasingly complex colloidal systems such as metallic, semiconductor, and biological particles, with noncollinear nonlinear light scattering spectroscopy.

ACKNOWLEDGMENTS

This work was funded by the Deutsche Forschungsgemeinschaft and is part of the research program of the Max-Planck Gesellschaft. The authors would like to thank Ralf Vogelgesang for useful discussions.

APPENDIX: QUADRUPOLAR BULK CONTRIBUTION

For centrosymmetric materials, the second-order dipole contribution vanishes and the higher-order terms include magnetic dipole and electric quadrupole contribution. Of these terms, the electric quadrupole can have a significant contribution. The nonlinear polarization derived from an electric quadrupole consists of a nonlocally excited dipole and a locally excited quadrupole contribution,[49]

$$\mathbf{P}_i = \chi^{(2)Q_1}_{ijkl}\boldsymbol{\nabla}_l[\mathbf{E}_{1,j}]\mathbf{E}_{2,k} + \chi^{(2)Q_2}_{ijkl}\mathbf{E}_{1,j}\boldsymbol{\nabla}_l[\mathbf{E}_{2,k}] - \boldsymbol{\nabla}_l[\chi^{(2)Q_0}_{ijkl}\mathbf{E}_{1,j}\mathbf{E}_{2,k}], \tag{A1}$$

where $\boldsymbol{\nabla}$ is the del operator ($\nabla_i = d/dx_i$) and the $\chi^{(2)Q_{0,1,2}}_{ijkl}$ are the relevant quadrupole susceptibility tensors. For an isotropic, centrosymmetric bulk, these tensors contain only the elements $\chi^{(2)Q_{0,1,2}}_{iijj}, \chi^{(2)Q_{0,1,2}}_{ijji}, \chi^{(2)Q_{0,1,2}}_{ijij}$ and $\chi^{(2)Q_{0,1,2}}_{iiii} = \chi^{(2)Q_{0,1,2}}_{iijj} + \chi^{(2)Q_{0,1,2}}_{ijji} + \chi^{(2)Q_{0,1,2}}_{ijij}$ (no summation over indices i and j). The resulting contraction $\mathbf{E}_0 \cdot \mathbf{P}$ then contains terms of the type $\mathbf{E}_0 \cdot \boldsymbol{\nabla}\mathbf{E}_1 \cdot \mathbf{E}_2$. In terms of vector spherical harmonics, the vector gradient diadic $\boldsymbol{\nabla}(j_{l'}(kr')\mathbf{Y}^m_{l,l'})$ can be expressed in tensor harmonics as defined by James,[53]

$$\boldsymbol{\nabla}[j_{l'}(kr')\mathbf{Y}^m_{l,l'}] = \frac{1}{2l'+1}[k(l')^{1/2}j_{l'-1}(kr')\mathbf{Y}^m_{l,l',l'-1} + k(l'+1)^{1/2}j_{l'+1}(kr')\mathbf{Y}^m_{l,l',l'+1}]. \tag{A2}$$

Here, $\mathbf{Y}^m_{l,l'}$ is a vector spherical harmonic, which is nonvanishing only for $|l'-l| \leq 1$. Equivalently $\mathbf{Y}^m_{l,l',l''}$ denote tensor spherical harmonics. The vector spherical harmonic $\mathbf{M}_{lm}$ and $\mathbf{N}_{lm}$ can be expressed in terms of this system as

$$\mathbf{M}_{lm}(r',\theta',\phi') = \frac{i}{l(l+1)}j_l(kr')\mathbf{Y}^m_{l,l}(\theta',\phi'), \tag{A3}$$

$$\mathbf{N}_{lm}(r',\theta',\phi') = (l+1)\left(\frac{l}{2l+1}\right)^{1/2} j_{l-1}(kr')\mathbf{Y}^m_{l,l-1}(\theta',\phi') - l\left(\frac{l+1}{2l+1}\right)^{1/2} j_{l+1}(kr')\mathbf{Y}^m_{l,l+1}(\theta',\phi'). \tag{A4}$$

Finally, the integral $\int \mathbf{E}_0 \cdot \boldsymbol{\nabla}\mathbf{E}_1 \cdot \mathbf{E}_2 d\Omega$ is expressed in terms of

$$\begin{aligned} Z^{m_0,m_1,m_2}_{l_0,\ldots,l'_2} &= \int \mathbf{Y}^{m_0}_{l_0,l'_0} \cdot \mathbf{Y}^{m_1}_{l_1,l'_1,l''_1} \cdot \mathbf{Y}^{m_2}_{l_2,l'_2} d\Omega \\ &= \frac{(-1)^{l'_0+l_1+l'_2}}{(4\pi)^{1/2}}(2l_0+1)^{1/2}(2l'_0+1)^{1/2}\ldots \\ &\quad \times (2l'_2+1)^{1/2}\begin{Bmatrix} l_0 & l'_0 & 1 \\ l''_1 & l'_1 & l_2 \end{Bmatrix}\begin{Bmatrix} l_1 & l'_1 & 1 \\ l'_2 & l_2 & l_0 \end{Bmatrix} \\ &\quad \times \begin{pmatrix} l'_0 & l''_1 & l'_2 \\ 0 & 0 & 0 \end{pmatrix}\begin{pmatrix} l_0 & l_1 & l_2 \\ m_0 & m_1 & m_2 \end{pmatrix}. \end{aligned} \tag{A5}$$

Combining the appropriate integrals and integrating over the particle radius then yields the electric quadrupole bulk contribution to the scattering pattern.

---

*debeer@mf.mpg.de
†roke@mf.mpg.de

[1] H. F. Wang, E. C. Y. Yan, E. Borguet, and K. B. Eisenthal, Chem. Phys. Lett. **259**, 15 (1996).
[2] N. Yang, W. E. Angerer, and A. G. Yodh, Phys. Rev. Lett. **87**, 103902 (2001).
[3] E. C. Y. Yan and K. B. Eisenthal, J. Phys. Chem. B **103**, 6056 (1999).
[4] E. C. Y. Yan and K. B. Eisenthal, Biophys. J. **79**, 898 (2000).
[5] Y. Jiang, P. T. Wilson, M. C. Downer, C. W. White, and S. P. Withrow, Appl. Phys. Lett. **78**, 766 (2001).
[6] E. C. Y. Yan, Y. Liu, and K. B. Eisenthal, J. Phys. Chem. B **105**, 8531 (2001).
[7] K. B. Eisenthal, Chem. Rev. **106**, 1462 (2006).
[8] R. K. Campen, D. S. Zheng, H. F. Wang, and E. Borguet, J. Phys. Chem. C **111**, 8805 (2007).
[9] H. F. Wang, T. Troxler, A. G. Yeh, and H. L. Dai, J. Phys. Chem. C **111**, 8708 (2007).

[10] L. Schneider, H. J. Schmid, and W. Peukert, Appl. Phys. B: Lasers Opt. **87**, 333 (2007).

[11] J. Martorell, R. Vilaseca, and R. Corbalan, Phys. Rev. A **55**, 4520 (1997).

[12] V. L. Brudny, B. S. Mendoza, and W. L. Mochán, Phys. Rev. B **62**, 11152 (2000).

[13] W. X. Xu, Opt. Laser Technol. **34**, 187 (2002).

[14] W. L. Mochán, C. López-Bastidas, J. A. Maytorena, B. S. Mendoza, and V. L. Brudny, Phys. Status Solidi B **240**, 527 (2003).

[15] S. Roke, W. G. Roeterdink, J. E. G. J. Wijnhoven, A. V. Petukhov, A. W. Kleyn, and M. Bonn, Phys. Rev. Lett. **91**, 258302 (2003).

[16] S. Roke, M. Bonn, and A. V. Petukhov, Phys. Rev. B **70**, 115106 (2004).

[17] V. L. Brudny, W. L. Mochán, J. A. Maytorena, and B. S. Mendoza, Phys. Status Solidi B **240**, 518 (2003).

[18] A. G. F. de Beer and S. Roke, Phys. Rev. B **75**, 245438 (2007).

[19] J. I. Dadap, Phys. Rev. B **78**, 205322 (2008).

[20] A. G. F. de Beer, H. B. de Aguiar, J. W. F. Nijsen, and S. Roke, Phys. Rev. Lett. **102**, 095502 (2009).

[21] G. S. Agarwal and S. S. Jha, Solid State Commun. **41**, 499 (1982).

[22] G. S. Agarwal and S. V. ONeil, Phys. Rev. B **28**, 487 (1983).

[23] X. M. Hua and J. I. Gersten, Phys. Rev. B **33**, 3756 (1986).

[24] C. A. Paddock, G. F. Russell, and R. B. Miles, Surf. Sci. **172**, 578 (1986).

[25] J. I. Dadap, J. Shan, K. B. Eisenthal, and T. F. Heinz, Phys. Rev. Lett. **83**, 4045 (1999).

[26] E. V. Makeev and S. E. Skipetrov, Opt. Commun. **224**, 139 (2003).

[27] J. I. Dadap, J. Shan, and T. F. Heinz, J. Opt. Soc. Am. B **21**, 1328 (2004).

[28] J. Nappa, G. Revillod, I. Russier-Antoine, E. Benichou, C. Jonin, and P. F. Brevet, Phys. Rev. B **71**, 165407 (2005).

[29] J. Nappa, I. Russier-Antoine, E. Benichou, C. Jonin, and P. F. Brevet, J. Chem. Phys. **125**, 184712 (2006).

[30] W. L. Mochán, J. A. Maytorena, B. S. Mendoza, and V. L. Brudny, Phys. Rev. B **68**, 085318 (2003).

[31] P. Figliozzi, L. Sun, Y. Jiang, N. Matlis, B. Mattern, M. C. Downer, S. P. Withrow, C. W. White, W. L. Mochán, and B. S. Mendoza, Phys. Rev. Lett. **94**, 047401 (2005).

[32] J. Shan, J. I. Dadap, I. Stiopkin, G. A. Reider, and T. F. Heinz, Phys. Rev. A **73**, 023819 (2006).

[33] Y. Pavlyukh and W. Hubner, Phys. Rev. B **70**, 245434 (2004).

[34] S. Roke, J. Buitenhuis, J. C. van Miltenburg, M. Bonn, and A. van Blaaderen, J. Phys.: Condens. Matter **17**, S3469 (2005).

[35] S. Roke, O. Berg, J. Buitenhuis, A. van Blaaderen, and M. Bonn, Proc. Natl. Acad. Sci. U.S.A. **103**, 13310 (2006).

[36] The former derive boundary conditions using effective charge and current distributions, while the latter derive boundary conditions directly from nonlinear polarization distribution. The two are equivalent if the effective charge (which corresponds to the radial component of nonlinear polarization) is isotropic. If this is not the case, the latter description takes precedence.

[37] L. D. Landau and E. M. Lifshitz, *Electrodynamics of Continuous Media* (Pergamon, Oxford, 1960).

[38] G. Mie, Ann. Phys. **25**, 377 (1908).

[39] P. Debye, Ann. Phys. **30**, 57 (1909).

[40] M. Kerker, *Scattering of Light and Other Electrodynamic Radiation* (Wiley, New York, 1969).

[41] M. Born and E. Wolf, *Principles of Optics* (Cambridge University Press, New York, 1997).

[42] J. D. Jackson, *Classical Electrodynamics* (Wiley, New York, 1975).

[43] C. F. Bohren and D. R. Huffman, *Absorption and Scattering of Light by Small Particles* (Wiley, New York, 1983).

[44] H. C. van de Hulst, *Light Scattering by Small Particles* (Wiley, New York, 1957).

[45] N. A. Gumerov and R. Duraiswami, J. Comput. Phys. **225**, 206 (2007).

[46] R. W. Boyd, *Nonlinear Optics* (Academic, New York, 1992).

[47] P. Butcher and D. Cotter, *The Elements of Nonlinear Optics* (Cambridge University Press, New York, 1990).

[48] P. Guyot-Sionnest and Y. R. Shen, Phys. Rev. B **38**, 7985 (1988).

[49] T. F. Heinz, *Nonlinear Surface Electromagnetic Phenomena* (Elsevier, New York, 1991), pp. 353–416.

[50] H. Held, A. I. Lvovsky, X. Wei, and Y. R. Shen, Phys. Rev. B **66**, 205110 (2002).

[51] W. M. Elsasser, Phys. Rev. **69**, 106 (1946).

[52] R. W. James, Pure Appl. Geophys. **111**, 2273 (1973).

[53] R. W. James, Philos. Trans. R. Soc. London, Ser. A **281**, 195 (1976).

[54] P. S. R. Diniz, E. A. B. D. Silva, and S. L. Netto, *Digital Signal Processing: System Analysis and Design* (Cambridge University Press, New York, 2002).

[55] W. Gan, D. Wu, Z. Zhang, R. R. Feng, and H. F. Wang, J. Chem. Phys. **124**, 114705 (2006).

[56] G. M. Hale and M. R. Querry, Appl. Opt. **12**, 555 (1973).